



Cite this: *J. Mater. Chem. C*,  
2024, 12, 14496

## Effects of loosely bound electrons and electron–phonon interaction on the thermoelectric properties of electrenes†

Yi-Ming Zhao,<sup>a</sup> Zishen Wang,<sup>b</sup> Jun Zhou,<sup>c</sup> Chun Zhang,<sup>de</sup>  
Sunmi Shin<sup>\*a</sup> and Lei Shen<sup>\*a</sup>

The low carrier mobility in conventional two-dimensional materials limits their thermoelectric (TE) applications due to high “density of scatterings”. Electrene, a new type of two-dimensional material has spatially interstitial electrons. These loosely bound electrons with a longer carrier–lattice distance undergo a weaker lattice perturbation, resulting in a higher mobility. Here, we systematically study the effect of loosely bound electrons, electron–phonon interaction, and spin orbital interaction on the TE properties of an electrene, HfI<sub>2</sub>, via first-principles calculations. We found that the p-type Seebeck coefficient is relatively large compared with those of other 2D materials with small effective mass. The larger hole relaxation time of HfI<sub>2</sub> results in high p-type electrical conductivity and power factor compared with n-type ones. It is found that the spin-orbital interaction splits the spin-degenerate bands near the Fermi level inducing a decrease of the bandgap and an increase of electrical conductivity. The electron–phonon interaction also affects the phonon transport which decreases the lattice thermal conductivity by 16% under the n-type doping. Overall, our high-fidelity calculations show that the maximum ZT value of HfI<sub>2</sub> reaches 1.12 at a temperature of 1200 K under p-type doping. Our work provides a physical picture of the effects of loosely bound electrons and their interaction with phonons and orbitals on thermoelectric properties, providing suggestions for further design of high-performance 2D thermoelectric materials.

Received 10th May 2024,  
Accepted 5th August 2024

DOI: 10.1039/d4tc01927j

rsc.li/materials-c

## 1 Introduction

Thermoelectric materials are promising for the conversion between heat and electricity in a clean and quiet way leveraging the transport by inside electrons and phonons in solids with no mechanical part like pistons and turbines.<sup>1,2</sup> The thermoelectric energy conversion efficiency is usually evaluated using the figure of merit,  $ZT (= S^2\sigma T/(\kappa_1 + \kappa_e))$ , where  $S$  is the Seebeck coefficient,  $\sigma$  is the electrical conductivity,  $T$  is the temperature,

$\kappa_e$  is the electron thermal conductivity and  $\kappa_1$  is the lattice thermal conductivity.<sup>3,4</sup> Ideal thermoelectric materials are usually narrow bandgap semiconductors with higher  $\sigma$  and low  $\kappa$  at the same time.<sup>5,6</sup> Two-dimensional (2D) thermoelectric materials are particularly suitable for wearable devices due to their flexible monolayer structure, which will supply electric power for other carried equipment.<sup>7,8</sup> However, the  $\sigma$  of 2D materials is usually lower compared with those of bulk structures because of the lower carrier mobility ( $\mu$ ) induced by a higher “density of scatterings”.<sup>9</sup> The electron density of states (DOS) is higher for 2D materials ( $D(E) = \text{constant}$ ) compared with the 3D case ( $D(E) \propto E^{1/2}$ ).<sup>10,11</sup> More phonons in a low energy range also increase the “density of scatterings”. Besides, the lattice thermal conductivity of 2D materials without inter-layer interaction is usually higher than that of bulk materials.<sup>12,13</sup> Thus, 2D semiconductors with high mobility and low thermal conductivity are favorable for thermoelectric applications.

The high carrier mobility and high Seebeck coefficient, unfortunately, seldom simultaneously coexist in a common individual material as a high  $S$  generally requires a large band effective mass or a small band curvature, but a high mobility

<sup>a</sup> Department of Mechanical Engineering, National University of Singapore, Singapore, 9 Engineering Drive 1, 117575, Singapore.  
E-mail: mpeshin@nus.edu.sg, shenlei@nus.edu.sg

<sup>b</sup> Department of NanoEngineering, University of California San Diego, 9500 Gilman Dr, La Jolla, CA 92093-0448, San Diego, 0448, USA

<sup>c</sup> Institute of Materials Research and Engineering (IMRE), Agency for Science, Technology and Research (A\*STAR), 2 Fusionopolis Way, Innovis, #08-03, 138634, Singapore

<sup>d</sup> Department of Physics, Faculty of Science, National University of Singapore, Singapore, 2 Science Drive 3, Blk S12, Level 2, 117551, Singapore

<sup>e</sup> Department of Chemistry, National University of Singapore, Singapore, Block S8 Level 3, 3 Science Drive 3, 117543, Singapore

† Electronic supplementary information (ESI) available. See DOI: <https://doi.org/10.1039/d4tc01927j>

requires a small band effective mass.<sup>14</sup> Recently, Zhang *et al.* found that several 2D structures including  $\text{HfI}_2$  and  $\text{ZrI}_2$  with a narrow bandgap exhibit a carrier mobility greater than  $4000 \text{ cm}^2 \text{ V}^{-1} \text{ s}^{-1}$  (the mobility of bulk Silicon is around  $1400 \text{ cm}^2 \text{ V}^{-1} \text{ s}^{-1}$ ).<sup>15</sup> For  $\text{HfI}_2$  and  $\text{ZrI}_2$  with a  $\text{MoS}_2$ -like structure (2H phase), there are excess electrons by checking the oxidation states (Hf and Zr: +4, I: −1) and these electrons are neither close to metal nor to halogen atoms but are distributed at the geometric center of hexagons.<sup>16</sup> Such a new type of 2D material with loosely bound electrons is also named electrene.<sup>17,18</sup> The interstitial electrons in the  $\text{HfI}_2$ -type structures undergo a weak lattice perturbation, resulting in a significantly high hole mobility. In addition, these interstitial electrons behave like quantum dots, of which the electron DOS should exhibit a sharp peak.<sup>19</sup> The Seebeck coefficient is relatively high because of the large energy derivative of the DOS according to the formula of the Seebeck coefficient from the Boltzmann transport equation (BTE).<sup>20</sup>

The higher lattice thermal conductivity of 2D materials is another shortcoming for achieving high thermoelectric energy conversion efficiency. The reported  $\kappa_l$  of another 2D electrene,  $\text{ZrI}_2$ , with only three-phonon (3ph) interactions is around  $20.3 \text{ W m}^{-1} \text{ K}^{-1}$  at room temperature.<sup>21</sup> The large atomic weight of Hf in the  $\text{HfI}_2$  structure will ensure a much lower lattice thermal conductivity compared with that of  $\text{ZrI}_2$ . Besides, the interstitial electrons also affect the phonon transport. The electron–phonon scattering decreases  $\kappa_l$  in structures like silicene and phosphorene.<sup>22</sup> Furthermore, Kim *et al.* reported that the cage structure  $12\text{CaO} \cdot 7\text{Al}_2\text{O}_3$ , a zero-dimensional (0D) electride with anionic electrons in the cage center, exhibits the characteristic of phonon glass and electron crystal (PGEC).<sup>23</sup> The concept of PGEC is a well-known strategy for the design of high-performance thermoelectric materials due to the coexistence of high  $\sigma$  and low  $\kappa_l$ .<sup>24</sup> 2D  $\text{HfI}_2$  with localized interstitial electrons is also a 0D electride according to the definition.<sup>25</sup> Overall, the 2D electrene,  $\text{HfI}_2$ , may have high  $S$ ,  $\sigma$  and low  $\kappa_l$ , favorable for the TE applications in flexible nanodevices. Currently, the electrene  $\text{HfI}_2$  has not been synthesized experimentally. But the electride structures like  $\text{Ca}_2\text{N}$  and  $\text{Y}_2\text{C}$  are synthesized and remain stable under the atmosphere of inert gases.<sup>26,27</sup> The 2D structures like black phosphorene are also synthesized and kept stably under the protection of inert BN in experiments.<sup>28</sup> Theoretical investigations on the thermoelectric properties will motivate experimental researchers to prepare electrene samples and examine their performance.

Here, we studied the thermoelectric properties of a 2D  $\text{HfI}_2$  structure with fully considering the effects of loosely bound electrons, spin-orbital interaction (SOI), and electron–phonon interaction (EPI). Our calculated results show that the p-type Seebeck coefficient is relatively high compared with those of some other high mobility 2D materials due to a high DOS peak at the valence band. The spin splitting induced by the SOI slightly decreases the bandgap and increases the carrier relaxation time. The maximum hole relaxation time reaches 0.7 ps, significantly higher than that of electrons due to the weaker lattice perturbation on charge states of the valence band

maximum (VBM). The p-type  $\sigma$  is also higher than the n-type value consistent with the higher hole relaxation time. The phonon relaxation time contributed by the electron–phonon scattering under electron doping is even smaller than that of the three-phonon scattering in a low phonon frequency range. As a result,  $\kappa_l$  decreases from 7.80 to  $6.58 \text{ W m}^{-1} \text{ K}^{-1}$  at an electron doping concentration of  $10^{14} \text{ cm}^{-2}$ . Our investigation helps to gain a better understanding about the effect of interstitial electrons on the thermoelectric properties of this 2D electrene system.

## 2 Computational methodology

We implemented the calculations based on density functional theory (DFT) to obtain the relaxed geometric structure and the electron band structure using the Quantum Espresso (QE) package.<sup>29</sup> The Perdew–Burke–Ernzerhof (PBE) functional is adopted to approximate the exchange–correlation of electrons.<sup>30</sup> The behavior of core electrons is approximated using norm-conserving pseudopotentials.<sup>31</sup> The spin-orbital interaction needs to be considered for the structures with heavy elements to obtain a more accurate electronic band structure.<sup>32,33</sup> We utilized the Heyd–Scuseria–Ernzerhof (HSE06) hybrid functional,<sup>34</sup> together with the SOI to calculate the electron band structure. The calculations of electron localization function and partial charge density are carried out using the Vienna ab initio simulation package (VASP).<sup>35</sup> The phonon properties are calculated based on the density functional perturbation theory (DFPT)<sup>36</sup> implemented using the ph.x code in the QE package.

To accurately evaluate the thermoelectric properties of the electrene structure, we need to calculate the carrier relaxation time from EPI. The electron and phonon transports are coupled due to the EPI, and the relaxation times of electrons ( $\tau_e$ ) and phonons ( $\tau_{\text{ph}}$ ) obtained from the EPI provide an effective way to decouple the electron and phonon transport behavior.<sup>37,38</sup> The  $\tau_e$  results from the EPI are significantly different from the constant one calculated based on deformation potential theory because  $\tau_e$  is not a constant value but varies with the chemical potential.<sup>39</sup> The investigation of the EPI for the 2D  $\text{HfI}_2$  structures will contribute to providing more accurate  $\tau_e$  and  $\tau_{\text{ph}}$  results, thereby revealing the effect of anionic electrons on the thermoelectric transport behavior. The EPI is investigated utilizing the electron–phonon Wannier (EPW) method based on the calculated electron and phonon properties.<sup>40</sup> The Fröhlich interaction is included to obtain a more accurate electron–phonon interaction and carrier relaxation time.<sup>41</sup> Then, the electrical conductivity, Seebeck coefficient, and electron thermal conductivity are calculated by solving the electron BTE with the BoltzTraP2 code<sup>42</sup> using the electron relaxation time obtained from EPW. The phonon BTE is solved to obtain the lattice thermal conductivity utilizing the ShengBTE code.<sup>43</sup> The detailed parameters like cut-off energy and the  $k$ -point mesh are listed in the ESI.† In addition, the lattice thermal conductivity under the effect of EPI is evaluated by the following

equation using the phonon group velocity ( $v$ ),  $\tau_{\lambda}^{\text{ph}}$  and frequencies ( $\omega$ ):

$$\kappa_1^{\alpha\beta} = \frac{1}{N_q V} \sum_{\lambda} \hbar \omega_{\lambda} \frac{\partial n_{\lambda}^0}{\partial T} v_{\lambda,\alpha} v_{\lambda,\beta} \tau_{\lambda}^{\text{ph}} \quad (1)$$

where  $\lambda$  is the phonon mode,  $n_{\lambda}^0$  is the Bose-Einstein distribution function, and  $\tau_{\lambda}^{\text{ph}}$  includes the interaction of three-phonon (3ph) ( $\tau_{\lambda}^{3\text{ph}}$ ) and electron-phonon ( $\tau_{\lambda}^{\text{el-ph}}$ ) following the Matthiessen's rule:

$$\frac{1}{\tau_{\lambda}^{\text{ph}}} = \frac{1}{\tau_{\lambda}^{3\text{ph}}} + \frac{1}{\tau_{\lambda}^{\text{el-ph}}} \quad (2)$$

$\tau_{\lambda}^{3\text{ph}}$  and  $\tau_{\lambda}^{\text{el-ph}}$  are obtained from the output of ShengBTE and EPW, respectively.

## 3 Results and discussion

### 3.1 Electron and phonon properties

We firstly evaluated the structural stability by checking the phonon band structure and lattice vibration in the *ab initio* molecular dynamics (AIMD) simulation process. There are no imaginary phonon frequencies inside the phonon band structure as shown in Fig. 1a, indicating that the atoms in 2D HfI<sub>2</sub> are in the lowest positions of the potential energy surface. The highest phonon frequency is only 185 cm<sup>-1</sup> (5.55 THz) because of the large atomic weight of the Hf and I elements. There is a small frequency gap between the acoustic and optical phonons, which will not strongly block the three-phonon interaction between these phonon modes. So, the four-phonon interaction will not influence the phonon transport significantly. Both the low maximum phonon frequency and small frequency gap should lead to a low  $\kappa_1$ . 2D HfI<sub>2</sub> is still stable at a temperature of 1200 K as the energy curve does not diverge after 8000 fs in AIMD simulations and the structure does not collapse as shown in Fig. 1b–d. Hence, the 2D HfI<sub>2</sub> structure should exist stably if synthesized successfully in the laboratory. The high temperature stability enables HfI<sub>2</sub> to work in a high temperature environment.

The electronic band structures are the basis for further investigation of the electron transport properties. We calculate

the electron and phonon properties based on the optimized monolayer structure with a lattice parameter of 3.77 Å. The bandgap reaches 0.77 eV when calculating with the PBE functional as shown in Fig. 2a. The DOS peak of the valence band around -1 eV is quite sharp as shown in Fig. 2b, which enhances the imbalance of DOS below and above the Fermi level under p-type doping. Then, the p-type Seebeck coefficient will be relatively large compared with those of other structures with small effective mass and small energy derivative of DOS near the band edges. The DOS near the CBM also changes rapidly with energy (large slope), indicating a high n-type Seebeck coefficient. The SOI leads to the splitting of spin degenerate bands near the VBM and the conduction band minimum (CBM), then the DOS at these band edges gets smaller. The bandgap value increases to 1.02 eV using the HSE06 functional together with SOI (HSE + SOI), close to the reported value.<sup>15</sup> Such a bandgap value will meet the requirements of narrow-bandgap semiconductors for thermoelectric applications.

The electron localization function (ELF) and charge density help to visualize the electronic structure more clearly. There are electrons distributed at the geometric center of the hexagon as shown in the ELF results in Fig. 2c, which indicates that the electrone HfI<sub>2</sub> is a 0D electride. The interstitial electrons are the intrinsic reasons for the sharp DOS peak near the VBM. The perturbation on the interstitial electrons from the lattice vibration is weaker compared with that on electrons close to the atoms due to the longer carrier-lattice distance. The VBM is occupied by the interstitial electrons as indicated by the decomposed charge density in Fig. 2d. Hence, the hole will transport much more easily, consistent with the large curvature of the highest valence band (small effective mass) and the reported high hole mobility results.<sup>15</sup>

### 3.2 Electron transport properties

We studied the EPI and obtained the carrier relaxation time based on the calculated electron and phonon band structures, as shown in Fig. 3a. The Fröhlich interaction greatly decreases the hole relaxation time near the VBM as shown in Fig. S1a (ESI<sup>†</sup>), which indicates that the interstitial charge is quite

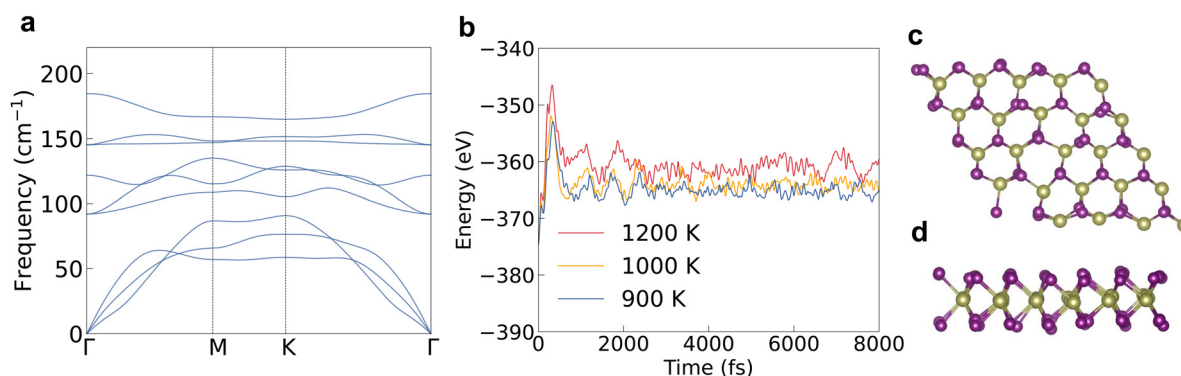


Fig. 1 (a) The phonon band structure of HfI<sub>2</sub>. (b) The variation of total energy from the *ab initio* molecular dynamics (AIMD) simulations at temperatures of 900, 1000 and 1200 K. (c) and (d) The top and side views of the structure during the AIMD simulation process at 1200 K.

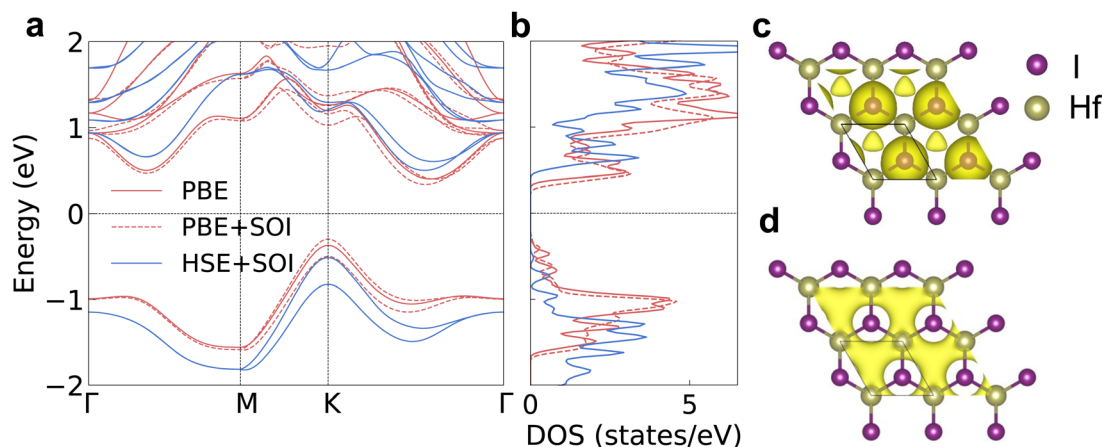


Fig. 2 (a) The electronic band structure calculated using the PBE functional, the PBE functional with SOI (PBE + SOI) and the HSE06 functional with SOI (HSE + SOI). (b) The total electron density of states corresponding to the band structure. (c) The electron localization function (ELF) with an isosurface value of 0.6. (d) The decomposed charge density of the highest valence band at the high-symmetry point *K* (an isosurface value of  $1.0 \times 10^{-2} \text{ e } \text{\AA}^{-3}$ ).

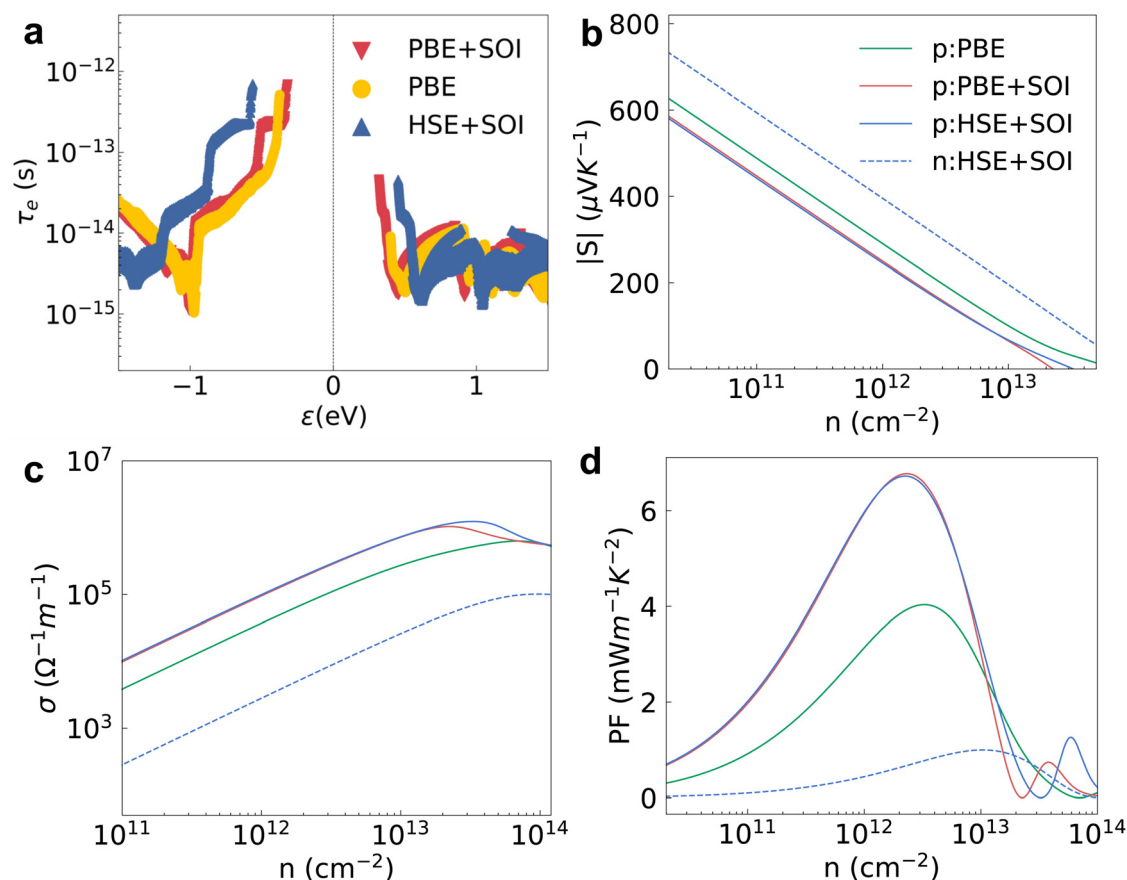


Fig. 3 (a) The electron relaxation time corresponding to different electron band structures. (b)–(d) The absolute value of the Seebeck coefficient, electrical conductivity and power factor corresponding to different band structures. The solid and dashed lines are these properties under p-type and n-type doping, respectively.

sensitive to the macroscopic electric field induced by longitudinal optical (LO) phonons.<sup>41</sup> Contrary to the holes, the relaxation time of electrons near the CBM is almost the same

regardless of whether the Fröhlich interaction is included or not.  $\tau_e$  near the VBM is reasonably higher than the value near the CBM because the interstitial charge near the VBM



undergoes a weaker lattice perturbation. The  $\tau_e$  near the VBM of HSE + SOI is almost the same compared with the value of PBE + SOI, although the electron bandgap calculated by the hybrid functional is larger (see Fig. 2). The hole mobility of 2D HfI<sub>2</sub> reaches 4854 cm<sup>2</sup> V<sup>-1</sup> s<sup>-1</sup> close to the published value (4782 cm<sup>2</sup> V<sup>-1</sup> s<sup>-1</sup>) as shown in Fig. S1b (ESI<sup>†</sup>), indicating that our calculations are reasonable.

Then, the electron BTE is solved based on the energy dependent carrier relaxation time. The carrier concentration is evaluated based on the rigid band approximation, which means the doping does not change the electron band structure strongly.<sup>42</sup> The transport properties at a smaller doping concentration are closer to the actual results. The transport properties for the 2H phase hexagonal HfI<sub>2</sub> structure are isotropic in-plane. Hence, there are no direction dependent values. The Seebeck coefficient value under p-type doping is around 300  $\mu$ V K<sup>-1</sup> at a carrier concentration of 10<sup>12</sup> cm<sup>-2</sup> under the PBE functional as shown in Fig. 3b, which is higher than the values of some other high mobility 2D materials like BSb.<sup>44</sup> The high  $S$  value under p-type doping is closely related to the VBM states occupied by interstitial electrons with a relatively sharp DOS peak. The  $S$  value under n-type doping is even higher due to the rapid change of DOS near the CBM. The SOI decreases the DOS near the VBM and the CBM due to the band splitting and the Seebeck coefficient value with SOI gets smaller than the value with only PBE as a result. The Seebeck coefficient under the hybrid functional is close to that under the PBE functional as the 0.77 eV bandgap of the PBE functional is already large enough to maintain the imbalance of charge carriers below and above the Fermi level. Unlike the Seebeck coefficient, the electrical conductivity is dominated by  $\tau_e$ . The p-type  $\sigma$  is much higher than the n-type one as shown in Fig. 3c, consistent with the higher  $\tau_e$  near the VBM.  $\sigma$  calculated by HSE + SOI is also close to that calculated by PBE + SOI due to similar  $\tau_e$ . The n-type Seebeck coefficients and electrical conductivity exhibit similar trends, *i.e.* SOI leads to a smaller Seebeck coefficient and larger electrical conductivity as shown in Fig. S2a and b (ESI<sup>†</sup>).

The power factor under p-type doping is much higher than that under n-type dominated by the higher p-type  $\sigma$  as shown in Fig. 3d. The PF values with SOI are higher than those without SOI, consistent with the larger electron relaxation time and electrical conductivity calculated using PBE + SOI and HSE + SOI. We also notice that the carrier concentration with peak PF value gets larger as the electrical conductivity gets smaller. With the full consideration of the EPI, SOI and hybrid functional, the maximum PF of HfI<sub>2</sub> reaches 6.72 mW m<sup>-1</sup> K<sup>-2</sup> under p-type doping at 300 K, while the corresponding n-type value is only 1.00 mW m<sup>-1</sup> K<sup>-2</sup> (Fig. S2c, ESI<sup>†</sup>). The carrier relaxation time has the greatest impact on the power factor values. The larger n-type Seebeck coefficient does not compensate for the small electrical conductivity which is mainly determined by the carrier relaxation time. The n-type PF value is much smaller than the p-type one as a result. We also calculated the electron band structure, ELF, carrier relaxation time, and p-type power factor of ZrI<sub>2</sub> for comparison. The electron properties of ZrI<sub>2</sub> are

similar to those of HfI<sub>2</sub>. Only the hole relaxation time and p-type power factor are slightly higher than the values of HfI<sub>2</sub> as shown in Fig. S3 (ESI<sup>†</sup>). The p-type PF value of HfI<sub>2</sub> is obviously higher than the values of 2D transition metal dichalcogenides (TMDCs) with MoS<sub>2</sub>-like structures.<sup>45</sup> For example, the experimentally measured PF of PtSe<sub>2</sub> is only 0.245 mW m<sup>-1</sup> K<sup>-2</sup>, highest among the reported PF values of TMDCs.<sup>46</sup> The electron thermal conductivity in Fig. S2d and S4 (ESI<sup>†</sup>) is proportional to the electrical conductivity according to the Wiedemann–Franz law.<sup>47</sup>

### 3.3 Phonon transport properties

The lattice thermal conductivity is another key factor for the thermoelectric properties, and is mainly determined by the phonon properties. From the calculated intermediate properties, the group velocity ( $v_g$ ) of low-frequency phonons, or acoustic phonons, is obviously larger than that of high-frequency optical phonons, as shown in Fig. 4a. The Grüneisen parameters ( $\gamma$ ) of low frequency phonons are quite large indicating a stronger lattice anharmonicity as shown in Fig. 4b. The lattice with a stronger anharmonicity usually exhibits lower thermal conductivity.<sup>48,49</sup> The loosely bound charge as indicated in Fig. 2d will soften the phonon modes and enhance the phonon anharmonicity, thereby decreasing the  $\kappa_l$ . Overall, the acoustic phonons will have a more dominant effect on the lattice thermal conductivity.

In the doped semiconductors, the phonons will interact with both other phonons and electrons. The phonon–phonon interaction is usually dominated by the three-phonon interaction (3ph) if the frequency gap between the acoustic and optical modes is not large enough.<sup>50</sup> The lattice thermal conductivity of HfI<sub>2</sub> reaches 7.80 W m<sup>-1</sup> K<sup>-1</sup> at 300 K if only the second and third order force constants are considered. The room temperature  $\kappa_l$  of HfI<sub>2</sub> is reasonably lower than the value of ZrI<sub>2</sub>, 20.30 W m<sup>-1</sup> K<sup>-1</sup>,<sup>21</sup> due to the heavier atomic weight of the Hf element. Limited by the higher lattice thermal conductivity, the final figure of merit of ZrI<sub>2</sub> will not be superior to HfI<sub>2</sub> as the power factor values of these two structures are similar. We notice the phonon scattering rate of the electron–phonon interaction under electron doping is even larger than that of the 3ph interaction for the phonon modes with frequencies around 50 cm<sup>-1</sup> as shown in Fig. 4c. The electron doping will scatter the phonons and enhance the phonon scattering rate due to the enhanced electron–phonon interaction by the high DOS near the CBM. Hence, the effect of EPI on the phonon transport should not be neglected especially under electron doping. The phonon scattering rate of 3ph and electron–phonon interaction is summed using the Matthiessen's rule. With the phonon frequencies, group velocity, and relaxation time from 3ph and EPI, we further calculate the lattice thermal conductivity with the contribution from EPI under electron doping. The electron doping with a concentration of 10<sup>14</sup> cm<sup>-2</sup> decreases the lattice thermal conductivity by 1.22 W m<sup>-1</sup> K<sup>-1</sup> at room temperature as shown in the cumulative  $\kappa_l$  in Fig. 4d. Contrary to the electron doping, the hole doping hardly affects the phonon scattering rate as shown in

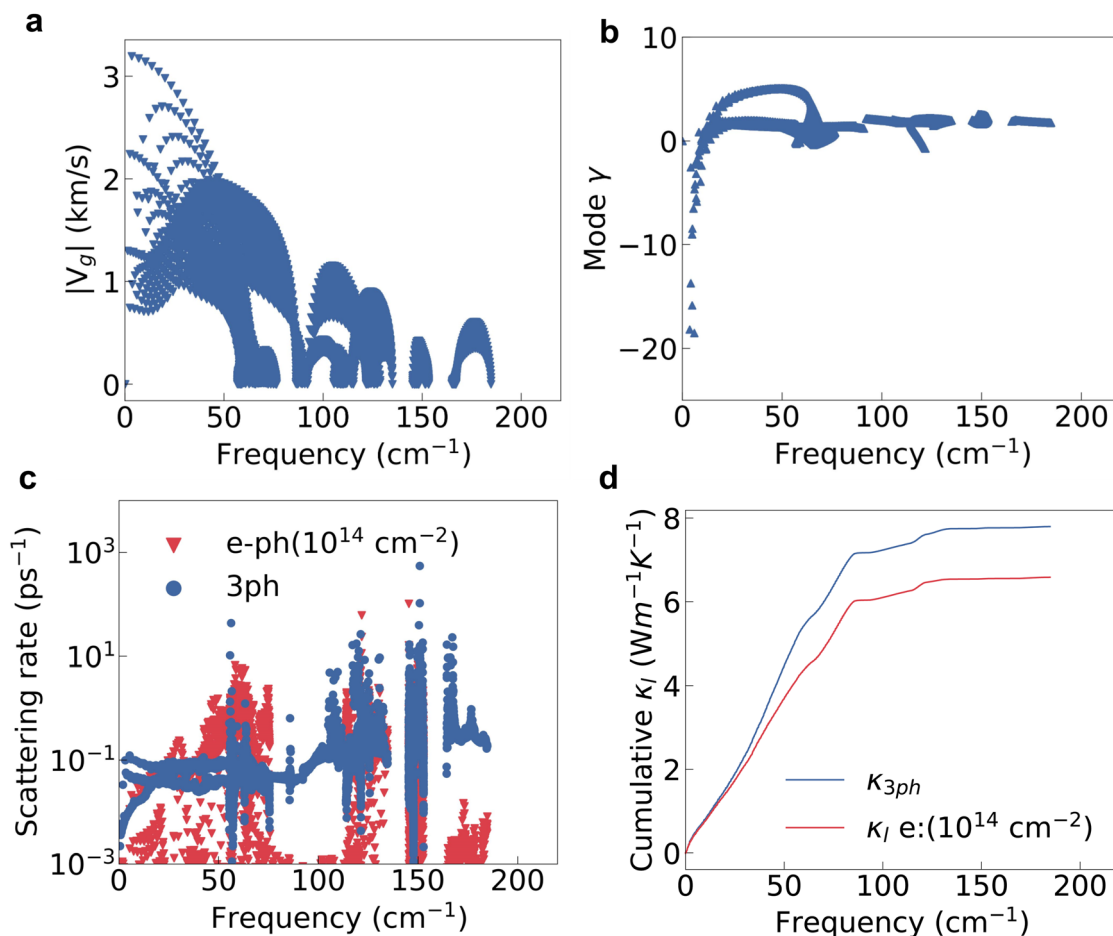


Fig. 4 (a) The phonon group velocity, (b) the Grüneisen parameter, (c) the phonon scattering rate contributed by 3ph and electron–phonon interactions at an electron concentration of  $10^{14}$  cm⁻² (e-ph( $10^{14}$  cm⁻²)), and (d) the cumulative lattice thermal conductivity with only the 3ph interaction and both 3ph and e-ph interactions.

Fig. S5 (ESI†) as the interstitial electrons induce a weak hole-phonon interaction.

### 3.4 Thermoelectric figure of merit

We also investigated the temperature effect on the electron-phonon and phonon-phonon interaction to evaluate the  $ZT$ . The lattice perturbation on the electron becomes stronger at higher temperature; then the electron relaxation time calculated by HSE + SOI gradually decreases as a result (see Fig. 5a). The hole mobility also decreases with the increasing temperature in an exponential trend as shown in Fig. S6a (ESI†). Contrary to the decreasing electron relaxation time and mobility, the Seebeck coefficient increases at higher temperatures as shown in Fig. S6b (ESI†). The electrical conductivity and electron thermal conductivity are dominated by the carrier relaxation time, which also decrease with increasing temperatures as shown in Fig. S6c and d (ESI†). The peak value of the p-type power factor at 1200 K is the smallest compared with the values at lower temperatures, which is consistent with the variation of  $\tau_e$  and  $\sigma$  as shown in Fig. 5b. Meanwhile, the lattice thermal conductivity decreases with increasing temperature as

shown in Fig. 5c. The effect of EPI on phonon transport is less sensitive to the temperature, and the  $\kappa_l$  value with only the 3ph interaction is almost the same compared with the value with both the 3ph and e-ph interaction at temperatures higher than 900 K.

The final thermoelectric figure of merit was evaluated with all the electron and phonon properties elaborated. Due to the decreasing of both the power factor and thermal conductivity, the  $ZT$  value increases with the increasing temperature. The decreasing  $\kappa_l$  under electron doping definitely does not contribute to improve the  $ZT$  under hole doping. The n-type  $ZT$  value at room temperature is only 0.041 at an electron concentration of  $10^{13}$  cm⁻² as shown in Fig. S7 (ESI†) even though  $\kappa_l$  is slightly smaller than the p-type one caused by the stronger EPI. The n-type Seebeck coefficient and electrical conductivity at 1200 K exhibit a strong bipolar effect and the peak  $ZT$  value is only 0.24 at an electron concentration of  $10^{14}$  cm⁻² (see Fig. S7d, ESI†). For p-type doping, we also calculate the bipolar thermal conductivity ( $\kappa_{bi}$ ) based on the electron and hole electrical conductivity and Seebeck coefficient.<sup>51</sup>  $\kappa_{bi}$  is just slightly smaller than the p-type  $\kappa_e$  and the final p-type  $ZT$  at

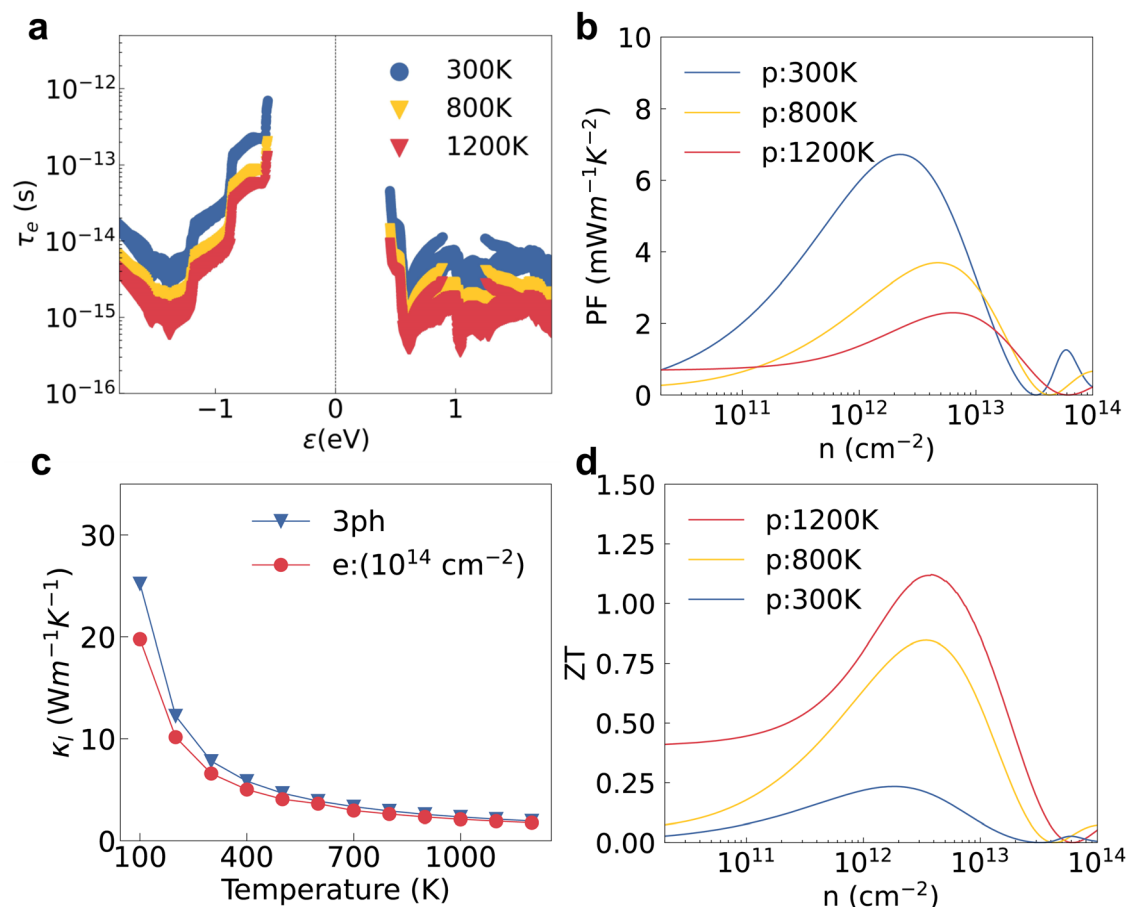


Fig. 5 (a) The electron relaxation time, (b) the power factor under p-type doping, (c)  $\kappa_l$  of the undoped structure and the  $\kappa_l$  values at an electron concentration of  $10^{14} \text{ cm}^{-2}$ , and (d) the final p-type ZT results at different temperatures.

1200 K decreases from 1.19 to 1.12 when the bipolar thermal process is included as shown in Fig. S8 (ESI<sup>†</sup>). The p-type ZT value at 1200 K is still higher than those at 800 K and 300 K as shown in Fig. 5d. The final ZT with a value of 1.12 at 1200 K is comparable to those of some 2D TMDCs like PtSe<sub>2</sub>.<sup>45</sup> Although the calculated ZT value of PtSe<sub>2</sub> reaches 0.84, the experimentally measured value is only 0.1 at room temperature.<sup>46,52</sup> Since our calculation method is high-fidelity, we believe the experimental ZT value of HfI<sub>2</sub> will be close to our calculated one. The ZT value can be further improved using several engineering approaches like doping, nanostructuring and interface engineering.<sup>53–56</sup>

## 4 Conclusion

In summary, we investigated the electron–phonon interaction and the thermoelectric properties of electrene HfI<sub>2</sub>. Its loosely bound interstitial electrons exhibit a high carrier relaxation time near the valence band maximum due to a weak lattice perturbation. The p-type Seebeck coefficient, although smaller than the n-type ones, is still relatively large due to the sharp DOS peak at the VBM occupied by the interstitial electrons. The hole mobility, p-type electrical conductivity, and power factor

are much higher than those of n-type. The inclusion of the spin orbital interaction and hybrid functional provides an accurate prediction of the Seebeck coefficient and electrical conductivity. The electron doping with a concentration of  $10^{14} \text{ cm}^{-2}$  decreases the lattice thermal conductivity by 16%. The final thermoelectric figure of merit reaches 1.12 at 1200 K under p-type doping. Our work suggests that electrenes, a new class of 2D materials, will be promising thermoelectric materials due to their unique electronic and phonon properties.

## Data availability

The data supporting this article have been included as part of the ESI<sup>†</sup>.

## Conflicts of interest

There are no conflicts of interest to declare.

## Acknowledgements

The authors thank Dr Jiaren Yuan, Dr Xiwen Zhang, and Dr Yongchao Rao for their helpful discussion. Y. M. Z. gratefully

acknowledges the support of China Scholarship Council (No. CSC202104910079). L. S. thanks the support from the Ministry of Education, Singapore, under its MOE Tier 1 (grant no. A-8001194-00-00). The computational work for this article was performed on resources of the National Supercomputing Centre, Singapore (<https://www.nscc.sg>) and the High Performance Computing of National University of Singapore (HPC@NUS IT).

## Notes and references

- 1 F. J. DiSalvo, *Science*, 1999, **285**, 703–706.
- 2 L. Xie, L. Yin, Y. Yu, G. Peng, S. Song, P. Ying, S. Cai, Y. Sun, W. Shi, H. Wu, N. Qu, F. Guo, W. Cai, H. Wu, Q. Zhang, K. Nielsch, Z. Ren, Z. Liu and J. Sui, *Science*, 2023, **382**, 921–928.
- 3 X.-L. Shi, J. Zou and Z.-G. Chen, *Chem. Rev.*, 2020, **120**, 7399–7515.
- 4 Y. Zhou and L.-D. Zhao, *Adv. Mater.*, 2017, **29**, 1702676.
- 5 M. Mukherjee, A. Srivastava and A. K. Singh, *J. Mater. Chem. C*, 2022, **10**, 12524–12555.
- 6 H. Shao, D. Ding, L. Zhang, C.-K. Dong and H. Zhang, *Mater. Today Phys.*, 2022, **27**, 100756.
- 7 K. Kanahashi, J. Pu and T. Takenobu, *Adv. Energy Mater.*, 2020, **10**, 1902842.
- 8 H. Huang, W. Li, C. Hu and X. Fan, *J. Mater. Chem. C*, 2023, **11**, 9449–9464.
- 9 L. Cheng, C. Zhang and Y. Liu, *Phys. Rev. Lett.*, 2020, **125**, 177701.
- 10 Y. Li, T. Ding, D. K. Sang, M. Wu, J. Li, C. Wang, F. Liu, H. Zhang and H. Xie, *J. Mater. Chem. C*, 2020, **8**, 4181–4191.
- 11 W. Li, S. Poncé and F. Giustino, *Nano Lett.*, 2019, **19**, 1774–1781.
- 12 G. Fugallo, A. Cepellotti, L. Paulatto, M. Lazzeri, N. Marzari and F. Mauri, *Nano Lett.*, 2014, **14**, 6109–6114.
- 13 L. Lindsay and D. A. Broido, *Phys. Rev. B: Condens. Matter Mater. Phys.*, 2012, **85**, 035436.
- 14 W. G. Zeier, A. Zevalkink, Z. M. Gibbs, G. Hautier, M. G. Kanatzidis and G. J. Snyder, *Angew. Chem., Int. Ed.*, 2016, **55**, 6826–6841.
- 15 C. Zhang, R. Wang, H. Mishra and Y. Liu, *Phys. Rev. Lett.*, 2023, **130**, 087001.
- 16 J. He, Y. Chen, Z. Wang, M. Yang, T. Yang, L. Shen, X. Xu, Y. Jiang, J. Chai, L. M. Wong, S. Wang, Y. P. Feng and J. Zhou, *J. Mater. Chem. C*, 2022, **10**, 7674–7679.
- 17 J. Zhou, Y. P. Feng and L. Shen, *Phys. Rev. B*, 2020, **102**, 180407.
- 18 J. Zhou, L. Shen, M. Yang, H. Cheng, W. Kong and Y. P. Feng, *Chem. Mat.*, 2019, **31**, 1860–1868.
- 19 M. S. Dresselhaus, G. Chen, M. Y. Tang, R. G. Yang, H. Lee, D. Z. Wang, Z. F. Ren, J. P. Fleurial and P. Gogna, *Adv. Mater.*, 2007, **19**, 1043–1053.
- 20 R. Sarabia Riquelme, Doctoral Dissertation, University of Kentucky, 2020.
- 21 J. Wen, J. Peng, B. Zhang and Z.-Y. Wang, *Nanoscale*, 2023, **15**, 4397–4407.
- 22 S.-Y. Yue, R. Yang and B. Liao, *Phys. Rev. B*, 2019, **100**, 115408.
- 23 S. W. Kim, R. Tarumi, H. Iwasaki, H. Ohta, M. Hirano and H. Hosono, *Phys. Rev. B: Condens. Matter Mater. Phys.*, 2009, **80**, 075201.
- 24 Z. Liu, J. Mao, S. Peng, B. Zhou, W. Gao, J. Sui, Y. Pei and Z. Ren, *Mater. Today Phys.*, 2017, **2**, 54–61.
- 25 S. Kanno, T. Tada, T. Utsumi, K. Nakamura and H. Hosono, *J. Phys. Chem. Lett.*, 2021, **12**, 12020–12025.
- 26 D. L. Druffel, K. L. Kuntz, A. H. Woomer, F. M. Alcorn, J. Hu, C. L. Donley and S. C. Warren, *J. Am. Chem. Soc.*, 2016, **138**, 16089–16094.
- 27 K. Lee, S. W. Kim, Y. Toda, S. Matsuishi and H. Hosono, *Nature*, 2013, **494**, 336–340.
- 28 S. C. Dhanabalan, J. S. Ponraj, Z. Guo, S. Li, Q. Bao and H. Zhang, *Adv. Sci.*, 2017, **4**, 1600305.
- 29 P. Giannozzi, O. Andreussi and T. Brumme, *et al.*, *J. Phys.: Condens. Matter*, 2017, **29**, 465901.
- 30 J. P. Perdew, K. Burke and M. Ernzerhof, *Phys. Rev. Lett.*, 1996, **77**, 3865–3868.
- 31 D. R. Hamann, *Phys. Rev. B: Condens. Matter Mater. Phys.*, 2013, **88**, 085117.
- 32 J. Li, Q. Yao, L. Wu, Z. Hu, B. Gao, X. Wan and Q. Liu, *Nat. Commun.*, 2022, **13**, 919.
- 33 J. Yuan, Y. Cai, L. Shen, Y. Xiao, J.-C. Ren, A. Wang, Y. P. Feng and X. Yan, *Nano Energy*, 2018, **52**, 163–170.
- 34 J. Heyd, G. E. Scuseria and M. Ernzerhof, *J. Chem. Phys.*, 2003, **118**, 8207–8215.
- 35 G. Kresse and J. Furthmüller, *Phys. Rev. B: Condens. Matter Mater. Phys.*, 1996, **54**, 11169.
- 36 S. Baroni, S. de Gironcoli, A. Dal Corso and P. Giannozzi, *Rev. Mod. Phys.*, 2001, **73**, 515–562.
- 37 J. Zhou, B. Liao and G. Chen, *Semicond. Sci. Technol.*, 2016, **31**, 043001.
- 38 Z. Bai, D. He, S. Fu, Q. Miao, S. Liu, M. Huang, K. Zhao, Y. Wang and X. Zhang, *Nano Sel.*, 2022, **3**, 1112–1122.
- 39 G. Samsonidze and B. Kozinsky, *Adv. Energy Mater.*, 2018, **8**, 1800246.
- 40 S. Poncé, E. R. Margine, C. Verdi and F. Giustino, *Comput. Phys. Commun.*, 2016, **209**, 116–133.
- 41 C. Verdi and F. Giustino, *Phys. Rev. Lett.*, 2015, **115**, 176401.
- 42 G. K. H. Madsen, J. Carrete and M. J. Verstraete, *Comput. Phys. Commun.*, 2018, **231**, 140–145.
- 43 W. Li, J. Carrete, N. A. Katcho and N. Mingo, *Comput. Phys. Commun.*, 2014, **185**, 1747–1758.
- 44 S. Ahmadi, M. Raeisi, L. Eslami and A. Rajabpour, *J. Phys. Chem. C*, 2021, **125**, 14525–14537.
- 45 R. Rani and M. M. Sinha, *Phys. Scr.*, 2024, **99**, 032002.
- 46 T.-Y. Su, T.-H. Wang and D. P. Wong, *et al.*, *Chem. Mater.*, 2021, **33**, 3490–3498.
- 47 A. Yadav, P. C. Deshmukh, K. Roberts, N. M. Jisrawi and S. R. Valluri, *J. Phys. Commun.*, 2019, **3**, 105001.
- 48 G. Qin, X. Zhang, S.-Y. Yue, Z. Qin, H. Wang, Y. Han and M. Hu, *Phys. Rev. B*, 2016, **94**, 165445.
- 49 F. Duan, C. Shen, H. Zhang and G. Qin, *Phys. Rev. B*, 2022, **105**, 125406.



- 50 X. Qian, J. Zhou and G. Chen, *Nat. Mater.*, 2021, **20**, 1188–1202.
- 51 J.-H. Bahk and A. Shakouri, *Appl. Phys. Lett.*, 2014, **105**, 052106.
- 52 J. Zhang, Y. Xie, Y. Hu and H. Shao, *Appl. Surf. Sci.*, 2020, **532**, 147387.
- 53 G. Wang, F. Meng, Y. Chen, A. Lotnyk and X. Shen, *Adv. Sci.*, 2024, **11**, 2308056.
- 54 J. Guo, Q. Ma, K. Luo, W. Qiu, H. Chen, P. Qian, Y. Deng, X. Wu, L. Yang and J. Tang, *Ceram. Int.*, 2024, **50**(9), 15209–15217.
- 55 V. C. S. Theja, V. Karthikeyan, D. S. Assi, H. Huang, V. Kannan, Y. Chen, C.-H. Shek and V. A. L. Roy, *Adv. Mater. Technol.*, 2024, 2301722.
- 56 J. Kim, W. Shim and W. Lee, *J. Mater. Chem. C*, 2015, **3**, 11999–12013.